Numerical study of the local behaviour of adhesive bonds under dynamic loading

Benjamin Vales, Steven Marguet, Romain Créac'Hcadec, Laurent Sohier, Jean-François Ferrero, Pablo Navarro

Numerical Study of the Local Behaviour of Adhesive Bonds under Dynamic Loading

B. Valès*[,a], S. Marguet[a], R. Créac'hcadec[b], L. Sohier[c], J.-F. Ferrero[a], P. Navarro[a]

[a] *Université de Toulouse, Institut Clément Ader (ICA), UMR CNRS 5312, UPS/INSA/ISAE/Mines Albi, 3 rue Caroline Aigle, F-31400 Toulouse, France*
[b] *ENSTA Bretagne, Institut de Recherche Dupuy de Lôme (IRDL), FRE CNRS 3744, ENSTA Bretagne/UBO/ENIB/UEB, 2 rue F. Verny, F-29806 Brest Cedex 9, France*
[c] *Université de Bretagne Occidentale, Institut de Recherche Dupuy de Lôme (IRDL), FRE CNRS 3744, ENSTA Bretagne/UBO/ENIB/UEB, 6 Avenue V. le Gorgeu - CS93837, F-29238 Brest Cedex 3, France*

*Corresponding author
Email address: benjamin.vales@univ-tlse3.fr (B. Valès)

Preprint submitted to Journal of Adhesion Science and Technology *January 13, 2016*

Numerical Study of the Local Behaviour of Adhesive Bonds under Dynamic Loading

Abstract

Nowadays, adhesively bonded structures are widely used in the transport sector for the development of lightweight vehicles. In order to guarantee passenger safety, it is thus necessary to understand the behaviour of such assemblies under dynamic and combined loadings. This paper presents a numerical study of the local behaviour of adhesively bonded assemblies under dynamic loading. In a first part, the ASTM D950-03 block impact test is studied. This device does not enable an homogeneous loading of the adhesive and causes stress concentrations. On the basis of existing quasi-static works, strategies are then implemented at a local scale. By combining a specific substrates geometry and by limiting the stiffness gradient between the substrates and the adhesive, results show that it is possible to obtain a qualitatively acceptable stress fields in the adhesive for mechanical characterization under dynamic loadings. The Arcan TCS device mentioned below, uses such solutions to characterize the mechanical behaviour of bonded joints subjected to combined quasi-static loadings. In this study, the question of its extensibility to dynamic loadings by the use of an impactor guided into a drop tower is investigated. A dedicated finite element model is built under the plane stress assumption. The stress distributions in the adhesive are analysed through time and space for several loading conditions. The stress versus time signals are then compared with the results coming from modal analysis in order to highlight the vibration behaviour of the device, directly linked to the configuration.

Keywords: Numerical analysis; Adhesive bonds; Impact behaviour; Arcan TCS device.

1. Introduction

Adhesively bonded joints are increasingly used in the transport industry in order to improve the design and reliability of structures of lightweight vehicles. Indeed, this assembly process offers an interesting alternative to mechanical and welded joints by providing many advantages such as the possibility to assemble two or more parts made of different materials (multi-materials assemblies : *e.g.* CFRP/Honeycomb sandwich), a better strength-to-weight ratio and design flexibility. However, such structures are subjected to complex impact conditions during their period of use (*e.g.* during a car accident). Hence, understanding the mechanical behaviour of these joints under dynamic and combined loadings appears to be a prerequisite to ensure user safety [1, 2].

Nowadays, several tests methods dedicated to the study of adhesively bonded joints are available under dynamic conditions [3–5]. The most commonly used are Izod and Charpy pendulums [6–9], Hopkinson bar techniques [10–13], drop weight machines [1, 14–16] and servo hydraulic systems [17, 18].

The standard test method for apparent shear strength of single-lap-joint adhesively bonded metal specimens by tension loading according to the ASTM D1002 [19] is very commonly used for the characterization of bond strength of adhesive joint under quasi-static loading. The single-lap joint (SLJ) geometry used for this test is also the most studied in dynamics [1, 4, 8, 9, 14, 15, 20] due to low production costs, its ease of implementation and its

similarity with geometry of many practical application [2, 3]. However, this type of test leads to three major difficulties if the aim is to develop a law of mechanical behaviour that can be implemented in a finite element code for simulation purposes: (1) Due to thin substrates, this test generates a complex mix of shear and normal stresses in the adhesive layer [2, 3, 21]. (2) Because of a high rigidity gradient between adhesive and substrates, a higher level of stress is concentrated at the ends of the overlap. This phenomenon is more commonly known as 'edge effects' and can generate cracks that initiate the failure of the test specimen [2, 22–24]. (3) This test is only used to characterize adhesive under a 'shear' loading. Its intrinsic drawbacks make its use interesting for comparative studies but not for material characterisation. Under quasi-static loadings, solutions were found: (a) To answer to the (1) difficulty, the Thick Adherend Shear Test (TAST) [25, 26] and modified TAST [27, 28] were developed by providing rigid substrates in order to limit the bending of the device. (b) Cognard and Créac'hcadec [22, 29] have shown that edge effects mainly depend of the ratio of the Young's modulus of the substrates and the adhesive and on the stiffness of the substrates. From these observations, they have developed test specimens with a specific geometry close to the adhesive that limit stress singularities (*i.e.* the (2) difficulty). (c) To test adhesives under combined loads, several assembly geometries can be used *e.g.* scarf-joint for tensile-shear test or butt-joint for compression and tensile test. Nevertheless, a specific specimen is required for each configuration. By using the geometry of the Arcan testing device developed by Arcan [30] and by drawing on (a) and (b) solutions, Cognard, Créac'hcadec *et al.* [31, 32] have developed a modified Arcan test. This one enables to circumvent the drawbacks of the SLJ geometry and stands out since it allows the study of joints under quasi-static combined loadings while minimizing the edge effects occurring in the adhesive [31–33].

To date, most of the dynamic studies on adhesive joints concerns the development of characterization or comparative tests. The present study focuses on the local behaviour of bonded joints subjected to combined dynamic loadings. In a first part, a numerical study of the local behaviour of the normalized ASTM D950-03 [6] block impact test is proposed. It reveals some edge effects near the ends of the joint. On the basis of existing quasi-static studies, strategies are then implemented to limit these edge effects. Thus, the influence of geometric and material parameters on the local mechanical response of bonded assemblies in dynamic combined loadings is investigated. Finally, an implementation of the local sample on a global scale is presented on an extension of the use of a modified Arcan device under drop weight dynamic conditions. Eventually, guidelines are drawn for an improved design of such a device.

2. Local study of the Standard Test Method for impact strength of adhesive bonds (ASTM D950-03)

2.1. Description

[Figure 1 near here]

The ASTM Block Impact Test D950-03 [6] is a pendulum test. It covers the determination of the comparative impact strength of adhesive bonds under shear loading. Figure 1 shows

the testing device and the specimen geometry. The jig shown in Fig.1a allows to hold the lower substrate of the test specimen. The upper one is free and impacted on one of its extremity by the impact head equipped with a flat striking face. The bonded area is 25.4 (length)×9.5 (width) ×0.2 mm (thickness) (see Fig.1b). The standard requires a hand velocity of $3.4\,\mathrm{m.s^{-1}}$.

2.2. Finite Element Analysis

[Figure 2 near here]

The 2D ASTM D950-03 finite element model shown in Fig.2 is designed to be faithful to the experimental device. The orthonormal coordinate system (O, $\underline{x}$, $\underline{y}$) is attached to the block impact test specimen and aligned with the adhesive. $\underline{y}$ corresponds to the thickness direction while $\underline{x}$ relates to the overlap direction (see Fig.2). We consider that the specimen is perfectly impacted (*i.e.* that the striking face is parallel to the impacted side of the specimen at the impact time) by a $m = 1\,\mathrm{kg}$ impact head of a pendulum with a initial velocity of $\|\underline{v}\| = 3.4\,\mathrm{m.s^{-1}}$. The axial loading is thus oriented along the direction $\underline{x}$. The concentrated mass of value m and the initial velocity induced by the fall of the head are imposed on a reference point of the finite element model (Master RP in Fig.2a). The latter is connected to some nodes of the impacted face (Slave nodes in magenta in Fig.2) by a rigid body relationship. Due to the large radius of the pendulum (in comparison with the size of the contact area), the edge composed of the slave nodes can move according to the rigid body kinematics, *i.e.* both translate along the direction $\underline{x}$ and rotate around $\underline{z}$. Between the lower edge of the striking face and the adhesive line, a gap $\delta = 0.5\,\mathrm{mm}$ is considered (see Fig.2b). On this interval, nodes are free. Nodes of the free edge of the lower substrate are clamped according to the adapter jig.

The geometry is meshed with CPS4R elements (4-node bilinear plane stress elements with reduced integration and hourglass control). A mesh convergence study has been performed to select the adequate element size. Because the stresses are theoretically infinite for elastic behaviour near the free edges (point A on Fig.2, see [24, 27] for details), the study has been carried out in the centre of the adhesive (point B on Fig.2), on the calculated values of σ_{xx}, σ_{yy} and σ_{xy} stresses. Thus the model contains 702 166 elements (1 408 160 DOF (2 DOF/node)) with 16 elements in the thickness of the adhesive. In order to analyse the stress distributions in the adhesive thickness, $h = 0$, $h = \pm e/2$ and $h = \pm e$ paths are respectively defined in the mid-plane, the 1/4-planes and the planes near the adhesive/substrates borders as shown in Fig.2b. Considered materials are an aluminium alloy and an epoxy adhesive. Typical values have been chosen for the mechanical properties. $E_a = 1.495\,\mathrm{GPa}$, $E_s = 70\,\mathrm{GPa}$, $\nu_a = 0.35$, $\nu_s = 0.34$, $\rho_a = 1\,100\,\mathrm{kg.m^{-3}}$ and $\rho_s = 2\,700\,\mathrm{kg.m^{-3}}$ define respectively the Young's modulus, the Poisson's ratio and the density of the adhesive and the substrates. These properties are the same all along the paper. The numerical analysis is performed under elastic and 2D plane stress assumptions. The finite element solution is obtained using the dynamic/explicit procedure (*i.e.* using the explicit time-integration algorithm) of Abaqus® [34]. [Figure 3 near here]

Fig.3 presents the normalized von Mises stresses in the block impact test specimen. Plots are extracted at an instant $t = 46\,\mu$s which corresponds to the moment when the maximum σ_{xy} stress value in the center of the overlap is reached. As shown in Fig.3a and b, the maximum von Mises stress value is obtained where the lower edge of the striking face hits the specimen (*i.e.* at $\delta = 0.5\,$mm from the upper adhesive line). Because the upper substrate is not guided along the $\underline{x}$-axis and the load is only applied to one of its faces (in the context of our study, the right one), this one tends to rotate around $\underline{z}$-axis. This observation can be confirmed by stress distributions in the adhesive extracted along the overlap joint and plotted on Fig. 4. Firstly, it is worth to notice that this test is not a pure shear test due to a significant presence of normal stresses. Also, Fig.4 clearly shows that stress fields are not homogeneous and both asymmetric along the overlap and through the thickness. At last, this one generates high stress concentrations at the ends of the overlap (*i.e.* $x \in [0\,\text{mm}, 0.4\,\text{mm}]$ and $x \in [25\,\text{mm}, 25.4\,\text{mm}]$) corresponding to the edge effects outlined in the introduction section. Likewise, magnitude of these ones increased in the vicinity of the interfaces substrates/adhesive. Thus, in this specific case, σ_{yy} is the predominant stress with a stress peak extracted from $h = e$ greater than 500 MPa in compression (it is recalled that the computation is made under pure elasticity assumptions, see Fig.4b). This observation demonstrates the major interest to reduce these unwanted effects in order to qualitatively characterize the adhesive of a bonded joint. [Figure 4 near here]

3. Effects of adhesive and adherend properties on stresses in adhesive joints under dynamic loading

3.1. Introduction

Edge effects phenomena have already been studied under quasi-static loading especially on single-lap joints and solutions were investigated [21, 22, 29, 35–38]. Thus, four methods appear to be effective:

(1) Change the substrates geometry near the ends of the joint;

(2) Change the adhesive geometry near the ends of the joint;

(3) Change the spew geometry;

(4) Decrease the ratio between the Young's moduli of the substrates and the adhesive.

Generally these strategies are mixed with the aim of finding an 'optimized shape'. In this section, the transposition under dynamic combined loadings of these quasi-static solutions is investigated by means of two studies: the local effects of adhesive and adherend geometries (by using the methods 1 to 3) and materials (by using the method 4).

3.2. Finite Element Model

[Figure 5 near here]

The finite element model used to perform these two studies (see Fig.5) allows to compare the relative influence of each parameter (*i.e.* geometric and material) on the local behaviour of the adhesive. The concerned model is composed of two rectangular substrates (in blue in

Fig.5) connected by an adhesive joint with a thickness of 0.2 mm (in red in Fig.5). We consider that the specimen is impacted by a falling mass guided by a drop tower of orthonormal coordinate system: (O, $\underline{x_0}$, $\underline{y_0}$). The resulting axial loading is oriented along the direction $\underline{y_0}$ of the gravitational force. The orthonormal coordinate system (O, $\underline{x}$, $\underline{y}$) is attached to the test specimen and aligned with the adhesive. $\underline{y}$ corresponds to the thickness direction while $\underline{x}$ relates to the overlap direction (see Fig.5a). At last, the angle $\gamma = (\underline{x_0}, \underline{x})$ measures the orientation of the specimen compared with the loading direction.
The same boundary conditions, materials and lap joint geometry as for the modelling of the block impact test are used in this section. Nodes of the lower edge of the lower substrate are clamped. Those of the upper edge of the upper substrates (named slave nodes in Fig.5a) are linked by a rigid body relationship to a reference point (named master RP in Fig.5a) which is in the centre of the edge. The concentrated mass of value m and the velocity induced by the falling of the weight are imposed on this point. Thus, slave nodes can only translate along the loading direction.
The geometry is meshed with CPS4R elements in the adhesive and a large area in the substrates (in dark blue and red in Fig.5) and CPS3 elements (3-node linear plane stress elements) elsewhere (in light blue in Fig.5). A mesh convergence study has been performed to select the adequate element size for each study. With the aim to analyse the stress distributions in the adhesive thickness, $h = 0$, $h = e/2$ and $h = e$ paths are respectively defined in the mid-plane, the 1/4-plane and the plane near the adhesive/upper-substrate border (see Fig.5b). The assumptions and the algorithm used for the modelling of the block impact test (plane stress, explicit time integration scheme and so on) are reused in this study.

3.3. Local effects of adhesive and adherend geometries

[Figure 6 near here]

Local effects of adhesive and adherend geometries are investigated in this section with a focus on inside taper configurations (Fig.6a, [2, 21]), chamfered beaks (Fig.6b, [22, 35]), filleted beaks (Fig.6c, [22, 29]) and shoulder filleted beaks (Fig.6d, [22]).
As for the block impact test study, the finite element models with straight-sided substrates and inside taper configurations highlight high stress singularities in the adhesive at the ends of the overlapping [23, 24]. Hence, mesh convergence is not reached for these configurations. However, in the case of the model with filleted beaks and $\alpha = 15\,^\circ$ the mesh convergence is clearly achieved in the entire adhesive. The difference in terms of peak stresses between a mesh with a critical element size of 0.0125 mm and 0.00625 mm is less than 2 % (in the worst case: extract from σ_{yy}, on $h = e$). This geometric study was therefore conducted by keeping the same reference mesh (with a critical element size of 0.0125 mm) in the adhesive for all cases. It enables a relative comparison between the technological solutions proposed to deal with edge effects.
Fig.7 presents the normal σ_{xx} and σ_{yy} (resp. in blue and red on Fig. 7) and shear σ_{xy} (in green on Fig. 7) stresses plotted along the overlap. For readability, data are extracted from $h = e$ (where the edge effects are highest as observed in Fig.4) for a shear loading test (*i.e.*, $\gamma = 90\,^\circ$). Normal $\sigma_{ii} = \underline{i}^T \boldsymbol{\sigma}_{(\mathbf{0}, \underline{\boldsymbol{x}}, \underline{\boldsymbol{y}})} \underline{i}$, $i = \{x, y\}$ and shear $\sigma_{xy} = \underline{x}^T \boldsymbol{\sigma}_{(\mathbf{0}, \underline{\boldsymbol{x}}, \underline{\boldsymbol{y}})} \underline{y}$ components of the stress tensor $\boldsymbol{\sigma}_{(\mathbf{0}, \underline{\boldsymbol{x}}, \underline{\boldsymbol{y}})}$ are extracted in the (O, $\underline{x}$, $\underline{y}$) specimen coordinate system at an

instant t which corresponds to the moment when the maximum value of σ_{xy} is reached. In order to compare all the data, stresses are normalized relatively to the value of σ_{xy} measured in the center of the overlap (*i.e.* $x = 12.7\,\text{mm}$). Thus, σ_{xy} is equal to one at the center of the adhesive. [Figure 7 near here]
In comparison with straight-sided substrates (*i.e.* $\alpha = 90\,^\circ$, dotted in Figs.7a-c), inside taper configurations allow to decrease the amplitude of the concentrated peaks (about 92 % of $\sigma_{yy}(\alpha = 90\,^\circ)$ for an inside taper with $\alpha = 15\,^\circ$, see Fig.7a). Nevertheless, it may be noticed that the $\alpha = 15\,^\circ$ inside taper gives better results than the $\alpha = 30\,^\circ$ one in terms of peaks reduction. Therefore, only a specific angle provides optimum results in term of low edge effects which depends in particular of the used materials. Moreover, this geometry tends to reduce the size of the loaded area: stresses are homogeneous along the overlap only between $x \in [3\,\text{mm}, 22.4\,\text{mm}]$, which corresponds to the non modified area. At the end of this modified area, new peaks of stresses appear as shown in Fig.7a.
According to Fig.7b, the use of chamfered beaks seems to be more interesting. In fact, it allows a significant decrease of the edge effects (about 83 % of $\sigma_{yy}(\alpha = 90\,^\circ)$ for a chamfered with $\alpha = 15\,^\circ$). The thinner are the beaks, the better are the peaks attenuations. The distribution is homogeneous and stable along the overlap. However, in this specific case of shear loading, Fig.7b shows that the use of chamfered beaks decrease the stress gradient $\frac{\partial \sigma_{xy}}{\partial x}$ near the edges of the joint (approximately equal to $0.2\,\text{mm}^{-1}$ (normalized stress) for $\alpha = 15\,^\circ$).
By combining filleted beaks and a small angle α (see Fig.7c), the chamfer efficiency is kept with regard to the edge effects and the stress gradient $\frac{\partial \sigma_{xy}}{\partial x}$ near the edges of the joint is greater. Thus, under shear loading, this geometry seems to be efficient because it reduces stress concentrations near the edges and allows to have a stable and homogeneous stress field in the adhesive. However, the thinness of the substrates at the edges makes this geometry of specimen very brittle and difficult to machine.
Leaving a shoulder between the bonding surface and the filleted beaks would enable to strengthen the specimen. Nonetheless, as it is shown in Fig.7d, beaks effects completely disappear with thick shoulder.

3.4. Local effects of adhesive and adherend materials

In this section, local effects of adhesive and adherend materials are investigated on specimens with $\alpha = 30\,^\circ$ filleted beaks (cf. Fig.7c) and under combined loadings. A ratio $\beta = E_s/E_a$, corresponding to the ratio between the Young's moduli of the substrates and the adhesive, is defined to analyse the edge effects.
Fig.8 presents the normal σ_{xx} and σ_{yy} (resp. in blue and red on Fig.8) and shear σ_{xy} (in green on Fig.8) stresses plotted along the overlap. Data are extracted from $h = e$ for a tensile ($\gamma = 0\,^\circ$, Fig.8a), a tensile-shear ($\gamma = 45\,^\circ$, Fig.8b), a shear ($\gamma = 90\,^\circ$, Fig.8c) and a compression-shear ($\gamma = 135\,^\circ$, Fig.8d) tests. Components of the stress tensor are extracted in the specimen coordinate system at an instant t which corresponds to the moment when the maximum value of stress is reached (value of σ_{xy} for a shear test, σ_{yy} for the others). In order to compare all the data, stresses are normalized relatively to the value of the maximum stress component σ_{max} (which depends on the loading case) measured in the center of the

overlap.
Whatever the loading case, two trend groups are clearly identified for each components of the stress tensor in Fig.8. The first (drawn with a thick line) corresponds to the results obtained with $\beta = 35$ and the second (drawn with a thin line) to those obtained with $\beta = 140$. In addition, under the assumptions presented in section 3.2, the impact of the materials properties on the stress distributions in the adhesive only depends on the ratio β.
Moreover, figures show that the edge effects are affected by a change of β: increasing its value also increases the stress concentrations magnitude near the edges. [Figure 8 near here]
Finally, by combining a specific substrates geometry with a low β, Fig.8 shows that it is possible to obtain homogeneous stress fields with no edge effects in the adhesive under dynamic combined loadings.
The same observations and results were found by Cognard, Créac'hcadec *et al.* [29, 31] under quasi-static assumptions. A remaining issue relates to the integration of this local sample into a testing device. To address this difficulty, the Arcan TCS specimen was developed. The investigation of its transposition to the case of dynamic loadings is therefore necessary and is the subject of the next section.

4. Local study of the Tensile/Compression - Shear Arcan test (Arcan TCS)

4.1. Global description

[Figure 9 near here]
The experimental Arcan TCS test presented in this section (shown in Fig.9) has been developed by Créac'hcadec *et al.* [29] with the aim to provide a reusable and easy to implement specimen dedicated to the characterization of the adhesive in an assembly. This device is composed of three parts: two metal substrates and an adhesive between them (resp. named A, B and C on Fig.9a). Four holes are machined on each substrates in order to test the bonded assembly under various loading cases. The bonded area is 25.4 (length)×9.5 (width) ×0.2 mm (thickness). During the manufacturing, the two substrates can be fixed together with two screws allowing to control their relative orientations and the thickness of the adhesive. Two filleted beaks forming an angle $\alpha = 30\,^\circ$ with the lap joint (see Fig.9c) are precision machined on the substrates in order to reduce the stress peaks occurring near the edges of the joint.

4.2. Finite Element Model

The 2D Arcan TCS finite element model shown in Fig.10 is designed to be faithful to the experimental device presented in section 4.1. However, some details of the specimen (*e.g.* the positioning holes) are not modelled in order to simplify the geometry to be meshed. We consider that the specimen is impacted by a falling mass guided by a drop tower of orthonormal coordinate system: (O, $\underline{x_0}$, $\underline{y_0}$). The resulting axial loading is thus oriented along the direction $\underline{y_0}$ of the gravitational force. The orthonormal coordinate system (O, $\underline{x}$, $\underline{y}$) is attached to the Arcan TCS test specimen and aligned with the adhesive. $\underline{y}$ corresponds to the thickness direction while $\underline{x}$ relates to the overlap direction (see Fig.10a). At last, the angle $\gamma = (\underline{x_0}, \underline{x})$ measures the orientation of the Arcan device compared with the loading

direction. Boundary conditions (Fig.10a) are applied on two opposite holes and are defined by their orientation γ. Thus, if $\gamma = 0\,^\circ$ (resp. $45\,^\circ$, $90\,^\circ$ and $135\,^\circ$), *i.e.* the mechanical loading is applied on the noted holes $0\,^\circ$ in Fig.10b (resp. $45\,^\circ$, $90\,^\circ$ and $135\,^\circ$), the loading case will be a tensile test (resp. a tensile-shear test, a shear test and a compression-shear test). In the following, these four cases are referred as conf. $0\,^\circ$, $45\,^\circ$, $90\,^\circ$ and $135\,^\circ$. A reference point is created at the center of each hole of the model and linked through a rigid body relationship to the slave nodes of the loaded half hole (in magenta in Fig.10a). Each configuration involves a lower reference point (lower RP in Fig. 10a) which can only rotate, and an opposite upper reference point (upper RP in 10a) which can both rotate around $\underline{z}$ axis and translate along the $\underline{y_0}$ direction of the drop tower. A concentrated mass of value m is associated to this latter one and models the mass of the impactor. At last, the initial velocity induced by the fall of the impactor, such as $\|\underline{v}\| = \underline{v} \cdot \underline{y_0}$, is imposed to the upper reference point. [Figure 10 near here]
The geometry is meshed with CPS4R elements in the adhesive and a small area in the substrates (in dark blue and red in Fig.10a and c) and CPS3 elements elsewhere (in light blue in Fig.10a and c, see Fig.10b). A mesh convergence study has been performed to select the adequate element sizes. Thus the model contains 401 626 elements (589 268 DOF (2 DOF/node)) with 16 elements in the thickness of the adhesive. With the aim to analyse the stress distributions in the adhesive thickness, $h = 0$, $h = e/2$ and $h = e$ paths are respectively defined in the mid-plane, the $1/4$-plane and the plane near the adhesive/upper-substrate border (see Fig.10c).

5. Dynamics results under elastic assumption

5.1. Stress distributions in the Arcan TCS specimen

Fig.11 presents the normalized von Mises stresses in the Arcan TCS test specimen for the four possible loading cases. Plots are extracted at an instant t which corresponds to the moment when the maximum von Mises stress is reached. Thus, for conf. $0\,^\circ$ (resp. $45\,^\circ$, $90\,^\circ$ and $135\,^\circ$), $t = 392\,\mu$s (resp. $t = 463\,\mu$s, $t = 776\,\mu$s and $t = 1\,219\,\mu$s). Results are obtained for a mass $m = 10\,$kg and an initial impact velocity $\|\underline{v}\| = 3.4\,\mathrm{m.s^{-1}}$. [Figure 11 near here]
Firstly, it may be noticed that the location of the maximum von Mises stress is not the same from case to case. In fact, for the tensile test, the maximum stress seems to be mainly concentrated near the holes used to hold the specimen. For the other tests, the maximum stress is located near the beaks in the connecting radius. The load path (*i.e.* the path taken by the stress wave) and its shape are also different from one case to another. Thus, the stress wave follows a straight line for the tensile and tensile-shear tests whereas it is more sinuous for the shear test and completely scattered for the compression-shear test (probably due to wave refraction against the free edges). Moreover, the stressed area is wider for the tensile test (approximately equal to the overlap length) than for the tensile-shear and shear tests (approximately equal to the half overlap length). Eventually, the stress fields observed for the tensile and tensile-shear tests are homogeneous unlike those observed for the shear and compression-shear ones. In these latter two cases, the stress wave propagates in unused

areas of the Arcan device which results in unwanted vibrations. It is therefore essential to analyse the spatial *vs* temporal stress distributions in the adhesive in order to provide an opinion on the use of this device under dynamic conditions.

5.2. Influence of the falling mass at constant kinetic energy

In this section, the influence of the falling mass upon the spatial *vs* temporal stress distributions, in the mid-plane (*i.e.* data extracted from $h = 0$) of the adhesive, is investigated at constant kinetic energy $K_c = 57.8\,\mathrm{J}$ set arbitrarily but in a realistic way. The two extreme cases of the tensile (Fig.12) and compression-shear (Fig.13) tests are examined. Normal σ_{ii}, $i = \{x, y\}$ and shear σ_{xy} components of the stress tensor $\boldsymbol{\sigma}_{(\mathbf{0},\underline{\boldsymbol{x}},\underline{\boldsymbol{y}})}$ are extracted in the (O, $\underline{x}$, $\underline{y}$) Arcan TCS coordinate system. Three useful configurations are analysed: (1) $m = 1\,\mathrm{kg}$ and $\|\underline{v}\| = 10.75\,\mathrm{m.s^{-1}}$ (in Figs.12a-c and 13a-c), (2) $m = 10\,\mathrm{kg}$ and $\|\underline{v}\| = 3.4\,\mathrm{m.s^{-1}}$ (in Figs.12d-f and 13d-f) and (3) $m = 50\,\mathrm{kg}$ and $\|\underline{v}\| = 1.52\,\mathrm{m.s^{-1}}$ (in Figs. 12g-i and 13g-i).
Fig.12 shows that only the normal stresses σ_{xx} and σ_{yy} are found in the adhesive for a tensile test, σ_{yy} being the predominant stress (greater than 600 MPa, due to elastic assumptions) and σ_{xy} being negligible compared to the two others. For the compression-shear test, all the components are found in the adhesive with σ_{yy} also being the predominant stress. Unlike in the tensile test, the mass of the impactor drives the maximum reached stress value. Thus, σ_{yy} evolves from $-300\,\mathrm{MPa}$ for a falling mass $m = 1\,\mathrm{kg}$ (see Fig.13b) to approximately $-200\,\mathrm{MPa}$ for heavier ones (see Fig.13e and h). The spatial distributions of the normal stresses along the overlap are quasi-homogeneous in the middle (*i.e.* $x \in [5\,\mathrm{mm}, 20.4\,\mathrm{mm}]$) whatever are the tests and the initial conditions. There is one noticeable exception for the compression-shear test with $m = 1\,\mathrm{kg}$. In this case, the stresses plotted in Fig.13a and b present some dissymmetry. Regarding the shear stress along the overlap, the spatial distributions are different. They have a second-order polynomial curve shape where the maximum value is reached in the center (*i.e.* $x \approx 12.7\,\mathrm{mm}$). For all cases, the spatial distributions of the stresses do not show any edge effects, thanks to the beaks and to the limited stiffness gradient between the substrates and the adhesive. Even if the temporal distributions of the shear stress in the adhesive for the tensile test seem to be noisy (12c, f and i) , the normal stresses are stables (*i.e.* without harmful oscillations). This observation can not be done for the compression-shear test where the temporal stress distributions are clearly affected by noise. This phenomenon is all the more important since the weight of the impactor is low. It is important to notice that under elastic and 2D plane stress numerical assumptions, only the falling mass has an influence on the shape of the spatial *vs* temporal distributions of the stresses in the adhesive. A modal analysis of the Arcan TCS specimen with the initial conditions investigated in this section and boundary conditions presented in the finite element model section is then required in order to understand the vibration response of the device under dynamic loadings. [Figure 12 near here] [Figure 13 near here]

5.3. Modal analysis of the Arcan TCS device

Fig.14 presents the results coming from the modal analysis of the Arcan TCS device for the tensile (Figs.14a and b) and the compression-shear tests (Figs.14c, d, e and f). Three

configurations are investigated: Figs.14a and b (resp. Figs.14c and d and Figs.14e and f) are associated to the $m = 10\,\text{kg}$ (resp. $m = 50\,\text{kg}$ and $m = 1\,\text{kg}$) and $\|\underline{v}\| = 3.4\,\text{m.s}^{-1}$ (resp. $\|\underline{v}\| = 1.52\,\text{m.s}^{-1}$ and $\|\underline{v}\| = 10.75\,\text{m.s}^{-1}$) initial tests conditions. For the compression-shear tests, the two studies carried out are focused on the two extreme cases presented in the previous section (the first with minor oscillations and the second affected by high magnitude noises). Fig.14a (resp. Fig.14c and Fig.14e) corresponds to the temporal distribution of σ_{yy} (resp. σ_{xy} and σ_{xy}, the stress the most affected by vibrations) and Fig.14b (resp. Fig.14d and Fig.14f) is associated to the vibrational spectrum. The latter is obtained by computing the modulus of the Fast Fourier Transform (FFT) of the signal. The vibration modes of the Arcan TCS device (in red dotted lines in Figs.14b, d and f) are calculated using the linear perturbation/frequency procedure of Abaqus® [34].
The vibrational spectrum which is associated to the tensile test (see Fig.14b) clearly shows that the only excited mode is the first one at $M_1 = 637,4\,\text{Hz}$. It corresponds to the fundamental mode, which is the testing mode.
The two other ones, which are associated to the compression-shear tests (see Fig.14d and f) also point the fundamentals respectively at $M_1 = 91.6\,\text{Hz}$ ($m = 50\,\text{kg}$) and at $M_1 = 627.9\,\text{Hz}$ ($m = 1\,\text{kg}$) but additional excited modes appear. With an impactor mass of $m = 50\,\text{kg}$ (see Fig.14d), the third mode is slightly excited at $M_3 = 5.771\,\text{kHz}$ (energy content 26 times lower than the fundamental). By decreasing its mass at $m = 1\,\text{kg}$ (see Fig.14f), about 6 additional modes are strongly excited, these with the greatest amplitude being the third and the eighth modes respectively at $M_3 = 5.803\,\text{kHz}$ and $M_8 = 21.04\,\text{kHz}$.
Fig.15 shows the displacements associated to the excited modes. Figs.15a and b are respectively associated to the fundamental modes of the tensile and compression-shear tests. Figs.15c and d respectively to the third and eighth modes of the compression-shear tests. The third one corresponds to the rotation of the device around its attachment points (noted holes 135 ° in Fig.10b, see Fig.15c). The eighth one to the rotation of the ends of the Arcan TCS device (Fig.15d). [Figure 14 near here] [Figure 15 near here]

6. Conclusions

From this study, three major conclusions can be drawn.
The first one is related to existing tests. Nowadays, numerous dynamic tests exist to compare the adhesive efficiency of bonded joints. Despite this, none of them seems to allow to know the mechanical behaviour of these joints under dynamic and combined loadings for simulation purposes.
The second conclusion is linked to the local effects of adhesive and adherend properties on the spatial distributions of the stresses and more particularly on the edge effects. Whatever the loading case, the use of beaks and of a limited stiffness gradient between the two substrates and the adhesive are as effective under dynamic than under quasi-static loadings.
The last conclusion concerns the use of the Arcan TCS device under dynamic loadings. The modal analysis has highlighted several vibration modes which are intrinsic to the configuration of the device. Fundamental modes are the wanted testing modes, whereas the upper modes are related to parasitic vibrations. For tensile and tensile-shear configurations, the

load path is quite direct between the boundary conditions and the adhesive joint. In these two specific cases, the Arcan TCS device gives satisfactory results in terms of spatial homogeneity of the stresses in the adhesive and temporal oscillations. In the other cases (*i.e.* shear and compression-shear configurations), the load path is more complex and causes both dissymmetry of the stress field in the adhesive and vibrations. In such cases, the adhesive is not uniformly solicited which can be an issue for its characterization. Concerning the boundary and initial conditions, the study shows that the choice of the mass of the impactor as well as the number of constraint degrees of freedom of the device have a significant impact on the behaviour of the assembly under dynamic loading. Thus a significant mass can help to control vibrations of the device but if it is too heavy, it could damage it. Some unwanted exited vibrations modes are directly linked to the rotation of the device around its attachment holes. The question of whether the device should be completely blocked must be treated.
Two main prospects appear from this study: (1) the achievement of an experimental campaign of tests, and (2), the development of suitable means of tests to characterize the dynamic behaviour of adhesive bonded joints under combined dynamic loads.

Acknowledgement

The authors acknowledge the supercomputing center CALMIP for granting access to the HPC resources under the allocation 2015-P09105 and F. Gilbert & D. Jacquet from ArcelorMittal, Montataire (France), for their financial support.

References

[1] Galliot C, Rousseau J, Verchery G. Drop weight tensile impact testing of adhesively bonded carbon/epoxy laminate joints. International Journal of Adhesion and Adhesives. 2012 Jun;35:68–75.
[2] Banea MD, da Silva LFM. Adhesively bonded joints in composite materials: An overview. Proceedings of the Institution of Mechanical Engineers, Part L: Journal of Materials Design and Applications. 2009;223(1):1–18.
[3] da Silva LFM, Adams RD, Blackman BRK, et al. Higher Rate and Impact Tests. In: Silva LFMd, Dillard DA, Blackman B, et al., editors. Testing Adhesive Joints. Wiley-VCH Verlag GmbH & Co. KGaA; 2012. p. 273–317.
[4] Galliot C. Static and dynamic behavior of adhesively bonded composite laminates. University of Burgundy; 2007.
[5] Goglio PL. Impact Tests. In: Silva LFMd, Achsner A, Adams RD, editors. Handbook of Adhesion Technology. Springer Berlin Heidelberg; 2011. p. 503–532.
[6] ASTMD950-03. Standard test method for impact strength of adhesive bonds. ASTM D950-03. 2011;.
[7] Adams RD, Harris JA. A critical assessment of the block impact test for measuring the impact strength of adhesive bonds. International Journal of Adhesion and Adhesives. 1996 May;16(2):61–71.
[8] Khalili SMR, Shokuhfar A, Hoseini SD, et al. Experimental study of the influence of adhesive reinforcement in lap joints for composite structures subjected to mechanical loads. International Journal of Adhesion and Adhesives. 2008 Dec;28(8):436–444.
[9] Goglio L, Rossetto M. Impact rupture of structural adhesive joints under different stress combinations. International Journal of Impact Engineering. 2008 Jul;35(7):635–643.
[10] Sato C, Ikegami K. Strength of Adhesively-Bonded Butt Joints of Tubes Subjected to Combined High-Rate Loads. The Journal of Adhesion. 1999 May;70(1-2):57–73.

[11] Goglio L, Peroni L, Peroni M, et al. High strain-rate compression and tension behaviour of an epoxy bi-component adhesive. International Journal of Adhesion and Adhesives. 2008 Oct;28(7):329–339.
[12] Raykhere SL, Kumar P, Singh RK, et al. Dynamic shear strength of adhesive joints made of metallic and composite adherents. Materials & Design. 2010 Apr;31(4):2102–2109.
[13] Yokoyama T, Nakai K. Determination of the impact tensile strength of structural adhesive butt joints with a modified split Hopkinson pressure bar. International Journal of Adhesion and Adhesives. 2015 Jan;56:13–23.
[14] Vaidya UK, Gautam ARS, Hosur M, et al. Experimental-numerical studies of transverse impact response of adhesively bonded lap joints in composite structures. International Journal of Adhesion and Adhesives. 2006 Jun;26(3):184–198.
[15] Pang SS, Yang C, Zhao Y. Impact response of single-lap composite joints. Composites Engineering. 1995;5(8):1011–1027.
[16] Higuchi I, Sawa T, Suga H. Three-dimensional finite element analysis of single-lap adhesive joints subjected to impact bending moments. Journal of Adhesion Science and Technology. 2002 Jan;16(10):1327–1342.
[17] Blackman BRK, Kinloch AJ, Taylor AC, et al. The impact wedge-peel performance of structural adhesives. Journal of Materials Science. 2000 Apr;35(8):1867–1884.
[18] Blackman BRK, Kinloch AJ, Rodriguez Sanchez FS, et al. The fracture behaviour of structural adhesives under high rates of testing. Engineering Fracture Mechanics. 2009 Dec;76(18):2868–2889.
[19] ASTMD1002-10. Standard Test Method for apparent shear strength of single-lap-joint adhesively bonded metal specimens by tension loading (metal-to-metal). ASTM D1002-10. 2010;.
[20] Park H, Kim H. Damage resistance of single lap adhesive composite joints by transverse ice impact. International Journal of Impact Engineering. 2010 Feb;37(2):177–184.
[21] F M da Silva L, D Adams R. Techniques to reduce the peel stresses in adhesive joints with composites. International Journal of Adhesion and Adhesives. 2007 Apr;27(3):227–235.
[22] Cognard JY. Numerical analysis of edge effects in adhesively-bonded assemblies application to the determination of the adhesive behaviour. Computers & Structures. 2008;86(17 to 18):1704 – 1717.
[23] Créac'hcadec R, Jamin G, Cognard JY, et al. Experimental analysis of the mechanical behaviour of a thick flexible adhesive under tensile/compression-shear loads. International Journal of Adhesion & Adhesives. 2014;48:258–267.
[24] Yosibash Z. Computing singular solutions of elliptic boundary value problems in polyhedral domains using the p-FEM. Applied Numerical Mathematics. 2000;33:7193.
[25] ASTMD3983-98. Standard Test Method for measuring strength and shear modulus of nonrigid adhesives by the thick-adherend tensile-lap specimen. ASTM D3983-98. 2011;.
[26] ISO11003-2. Adhesives-Determination of shear behaviour of structural adhesives-Part 2: Tensile test method using thick adherends. ISO 11003-2. 2011;.
[27] Cognard JY, Créac'hcadec R, Sohier L, et al. Influence of adhesive thickness on the behaviour of bonded assemblies under shear loadings using a modified TAST fixture. International Journal of Adhesion and Adhesives. 2010 Jul;30(5):257–266.
[28] Cognard JY, Créac'hcadec R, Sohier L, et al. Analysis of the nonlinear behavior of adhesives in bonded assemblies - Comparison of TAST and Arcan tests. International Journal of Adhesion and Adhesives. 2008 Dec;28(8):393–404.
[29] Créac'hcadec R, Sohier L, Cellard C, et al. An Arcan Tensile Compression Shear Test reducing the edge effects suited for the determination of the Load-Displacement Behaviour of Adhesives in Bonded Assemblies. International Journal of Adhesion and Adhesives. 2015;Accepted.
[30] Arcan L, Arcan M, Daniel L. SEM fractography of pure and mixed mode interlaminar fracture in graphite/epoxy composites. ASTM Technical Publication, Philadelphia. 1987;948:41–67.
[31] Cognard JY, Davies P, Sohier L, et al. A study of the non-linear behaviour of adhesively-bonded composite assemblies. Composite Structures. 2006;76:34–46.
[32] Cognard JY, Davies P, Gineste B, et al. Development of an improved adhesive test method for composite assembly design. Composite Science and Technology. 2005;65:359–368.

[33] Cognard JY, Créac'hcadec R. Analysis of the non linear behaviour of an adhesive in bonded assemblies under shear loadings. Proposal of an improved TAST test. Journal of Adhesion Science and Technology. 2009;23:1333–1355.
[34] Abaqus 6.12 Documentation. Providence, RI, USA; 2012.
[35] Belingardi G, Goglio L, Tarditi A. Investigating the effect of spew and chamfer size on the stresses in metal/plastics adhesive joints. International Journal of Adhesion and Adhesives. 2002;22(4):273–282.
[36] Kaye RH, Heller M. Through-thickness shape optimisation of bonded repairs and lap-joints. International Journal of Adhesion and Adhesives. 2002;22(1):7–21.
[37] Lang TP, Mallick PK. Effect of spew geometry on stresses in single lap adhesive joints. International Journal of Adhesion and Adhesives. 1998 Jun;18(3):167–177.
[38] Rispler AR, Tong L, P Steven G, et al. Shape optimisation of adhesive fillets. International Journal of Adhesion and Adhesives. 2000;20(3):221–231.

List of Figures

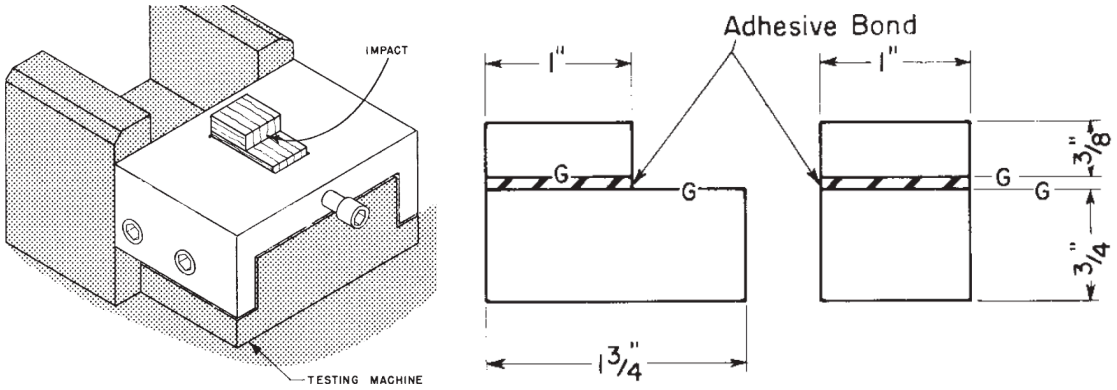

(a) (b)

Figure 1: Description of the ASTM D950-03 Test [6]. (a) Adapter jig for impact machines. (b) Block shear impact test specimens.

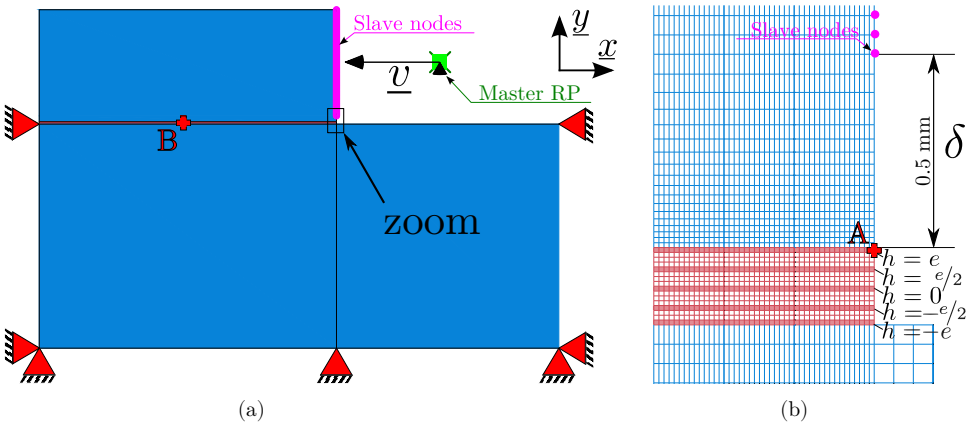

(a) (b)

Figure 2: Description of the ASTM D950-03 Test finite element model. (a) Boundary conditions. (b) Zoom on the mesh near the right edge of the adhesive joint.

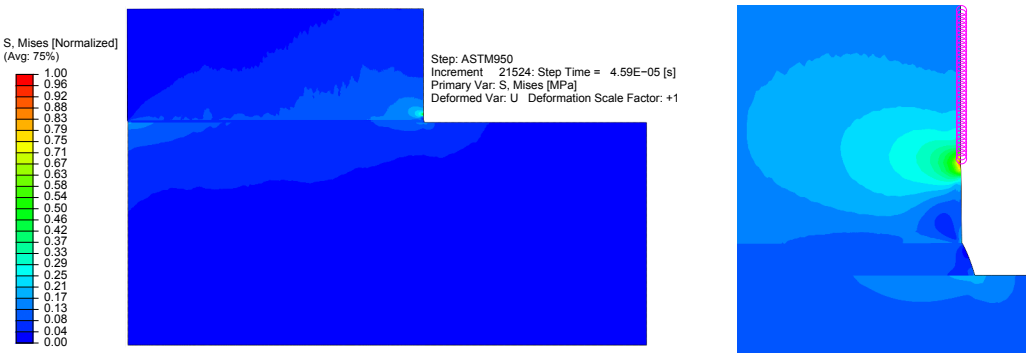

(a) (b)

Figure 3: von Mises stresses in the block shear impact test specimen. (a) Global view. (b) Zoom near the right edge of the adhesive joint.

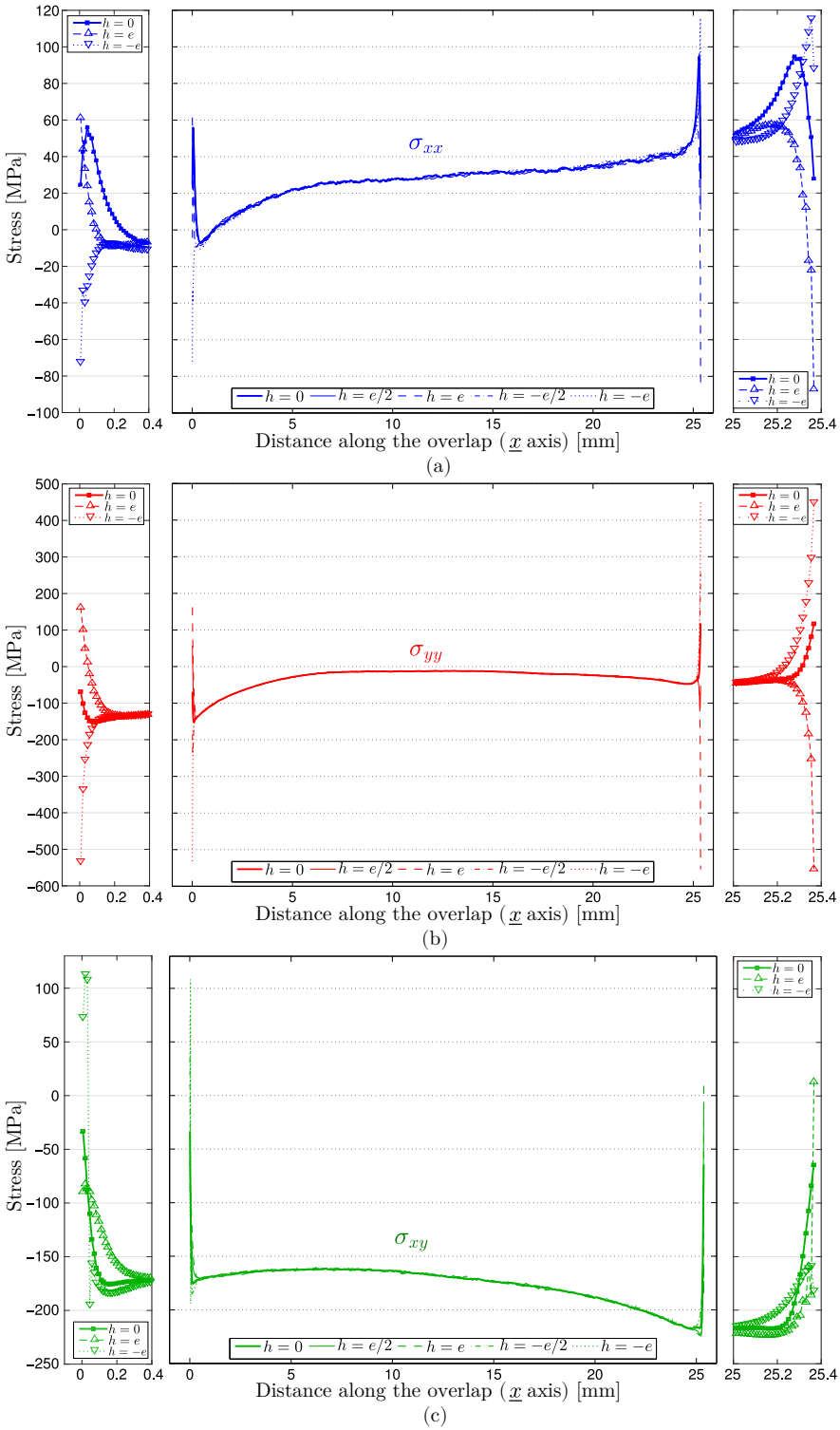

Figure 4: Stress distributions in the adhesive (extracted from $h = \{-e, -e/2, 0, e/2, e\}$) along the overlap and zoom on the associated edge effects near the right and left edges of the adhesive joint. (a) σ_{xx} distributions. (b) σ_{yy} distributions. (c) σ_{xy} distributions.

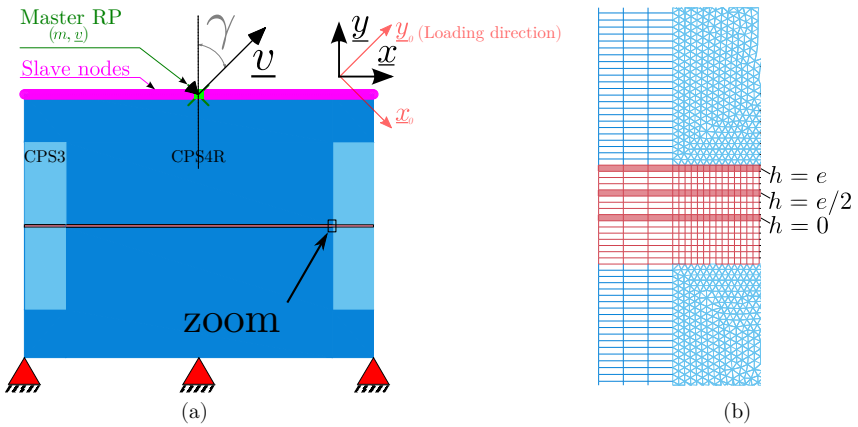

Figure 5: Description of the local finite element model. (a) Boundary conditions. (b) Zoom on the mesh near the border CPS4R/CPS3 elements.

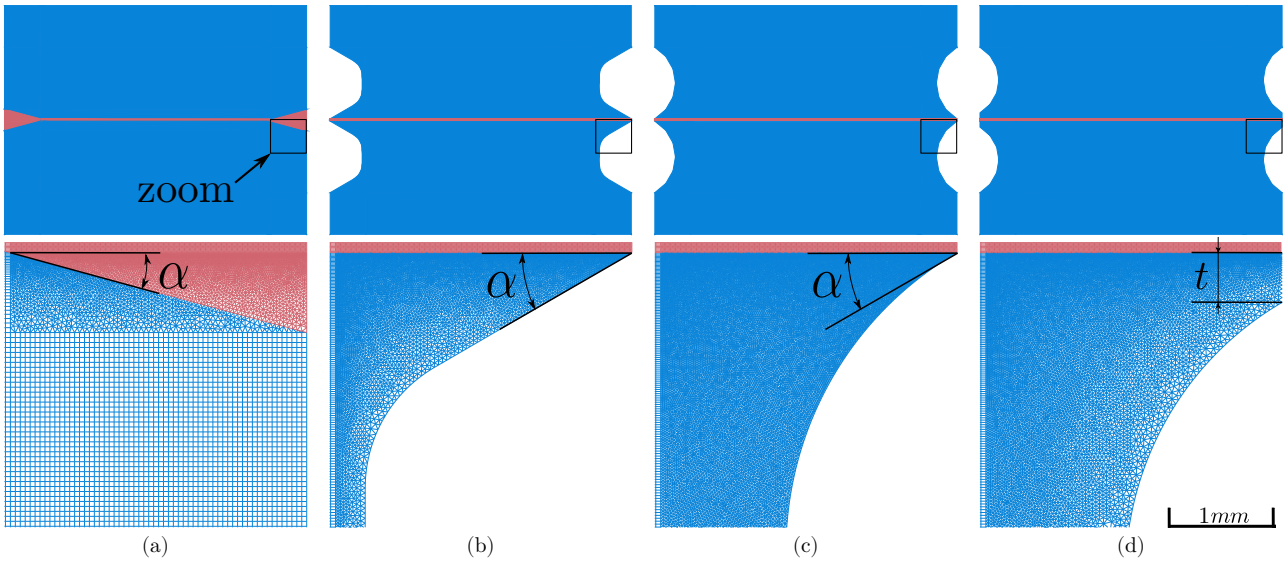

Figure 6: Presentation of the tested beaks geometries and their local zoom on the mesh. (a) Inside taper configuration. (b) Chamfered beaks. (c) Filleted beaks. (d) Shoulder filleted beaks.

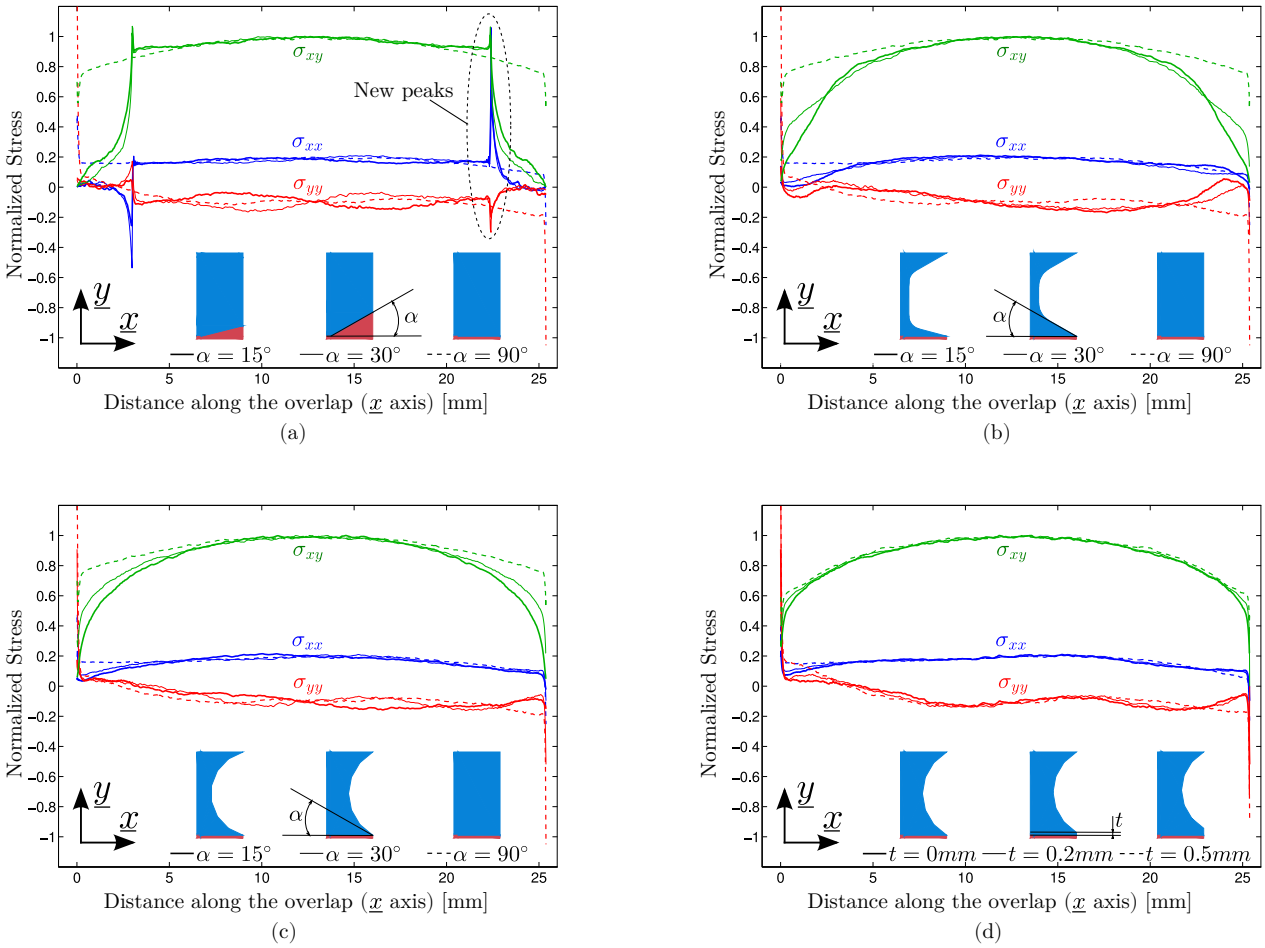

Figure 7: Stress distributions near the interface upper-substrate/adhesive ($h = e$) for four different geometries of beak. (a) Inside taper configurations with different angles $\alpha = \{15\,°, 30\,°, 90\,°\}$. (b) Chamfered beaks with different angles $\alpha = \{15\,°, 30\,°, 90\,°\}$. (c) Filleted beaks with different angles $\alpha = \{15\,°, 30\,°, 90\,°\}$. (d) Shoulder filleted beaks with different shoulder thicknesses $t = \{0\,\text{mm}, 0.1\,\text{mm}, 0.2\,\text{mm}\}$.

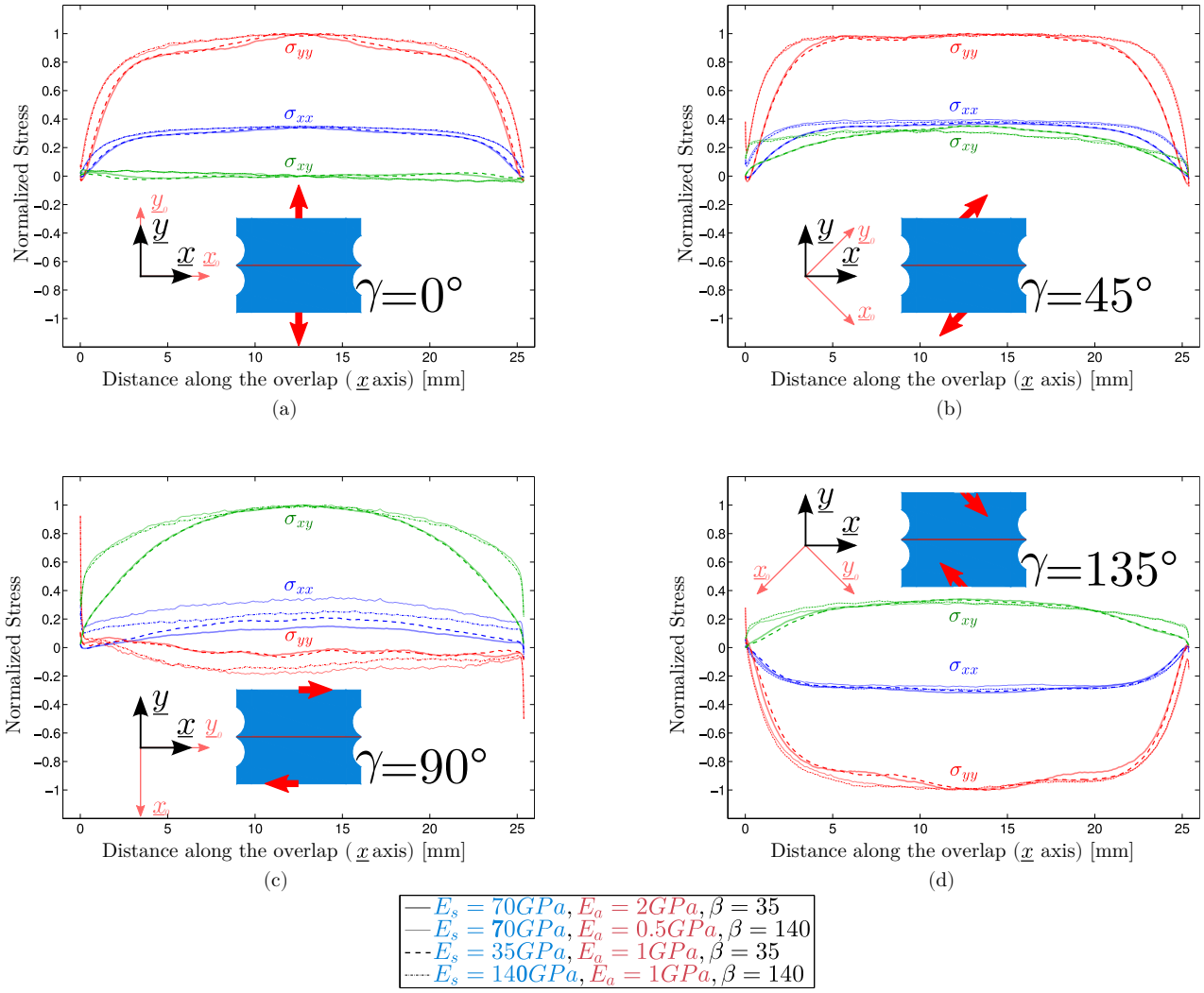

Figure 8: Stress distributions near the interface upper-substrate/adhesive ($h = e$) for different ratio $\beta = E_s/E_a$ in the case of filleted beaks with an angle $\alpha = 30\,^\circ$. (a) Results for the tensile test ($\gamma = 0\,^\circ$). (b) Results for the tensile-shear test ($\gamma = 45\,^\circ$). (c) Results for the shear test ($\gamma = 90\,^\circ$). (d) Results for the compression-shear test ($\gamma = 135\,^\circ$).

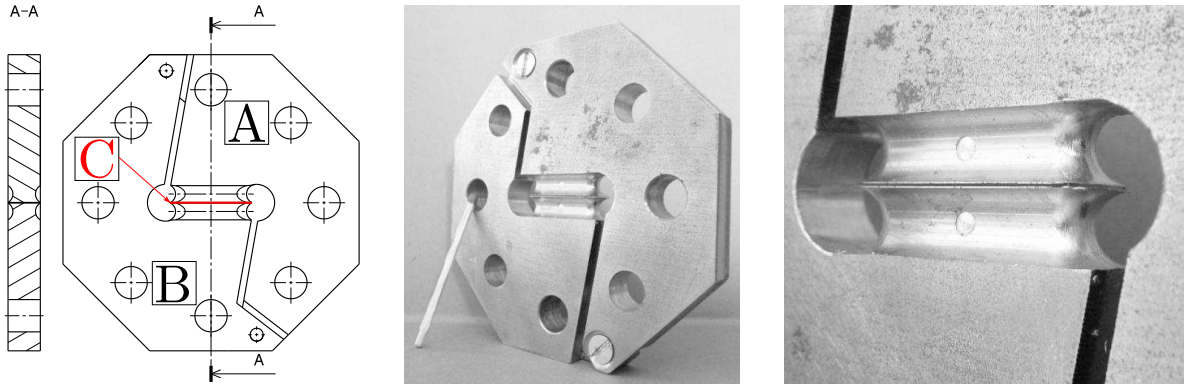

(a) (b) (c)

Figure 9: Tensile/Compression-Shear Arcan Test. (a) Technical drawing. (b) General view of the test specimen [29]. (c) Zoom on the local geometry of the beaks [29].

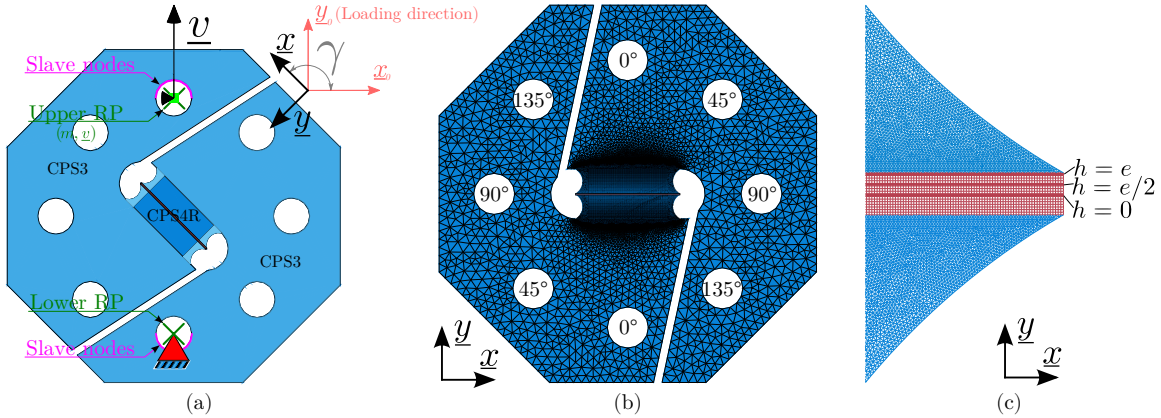

Figure 10: Description of the ARCAN TCS finite element model. (a) Boundary conditions. (b) Global mesh. (c) Zoom on the mesh near the right edge of the adhesive joint.

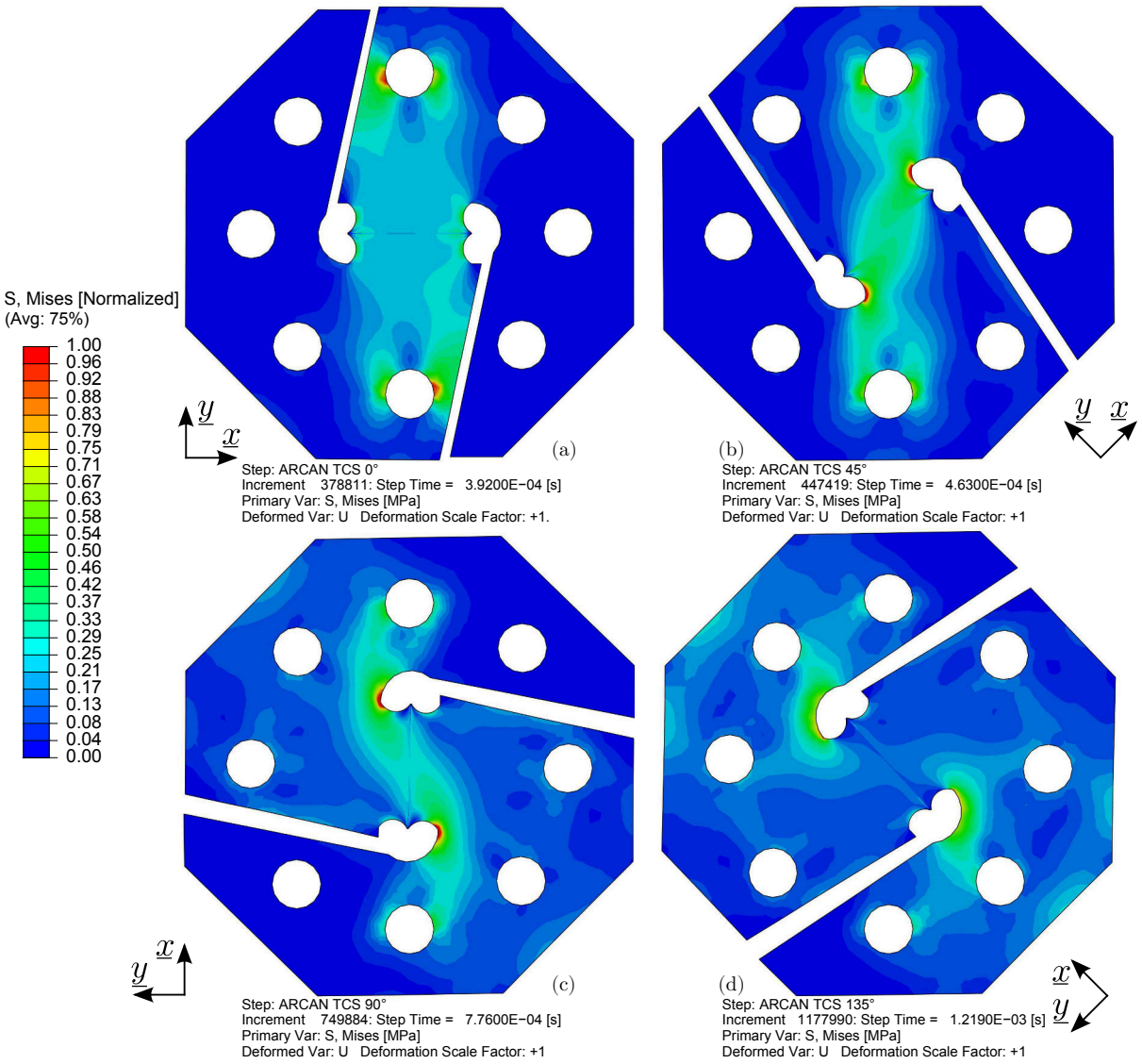

Figure 11: Normalized von Mises stresses in the ARCAN TCS test specimen for four loading cases. (a) Tensile test ($\gamma = 0\,^\circ$). (b) Tensile-shear test ($\gamma = 45\,^\circ$). (c) Shear test ($\gamma = 90\,^\circ$). (d) Compression-shear test ($\gamma = 135\,^\circ$).

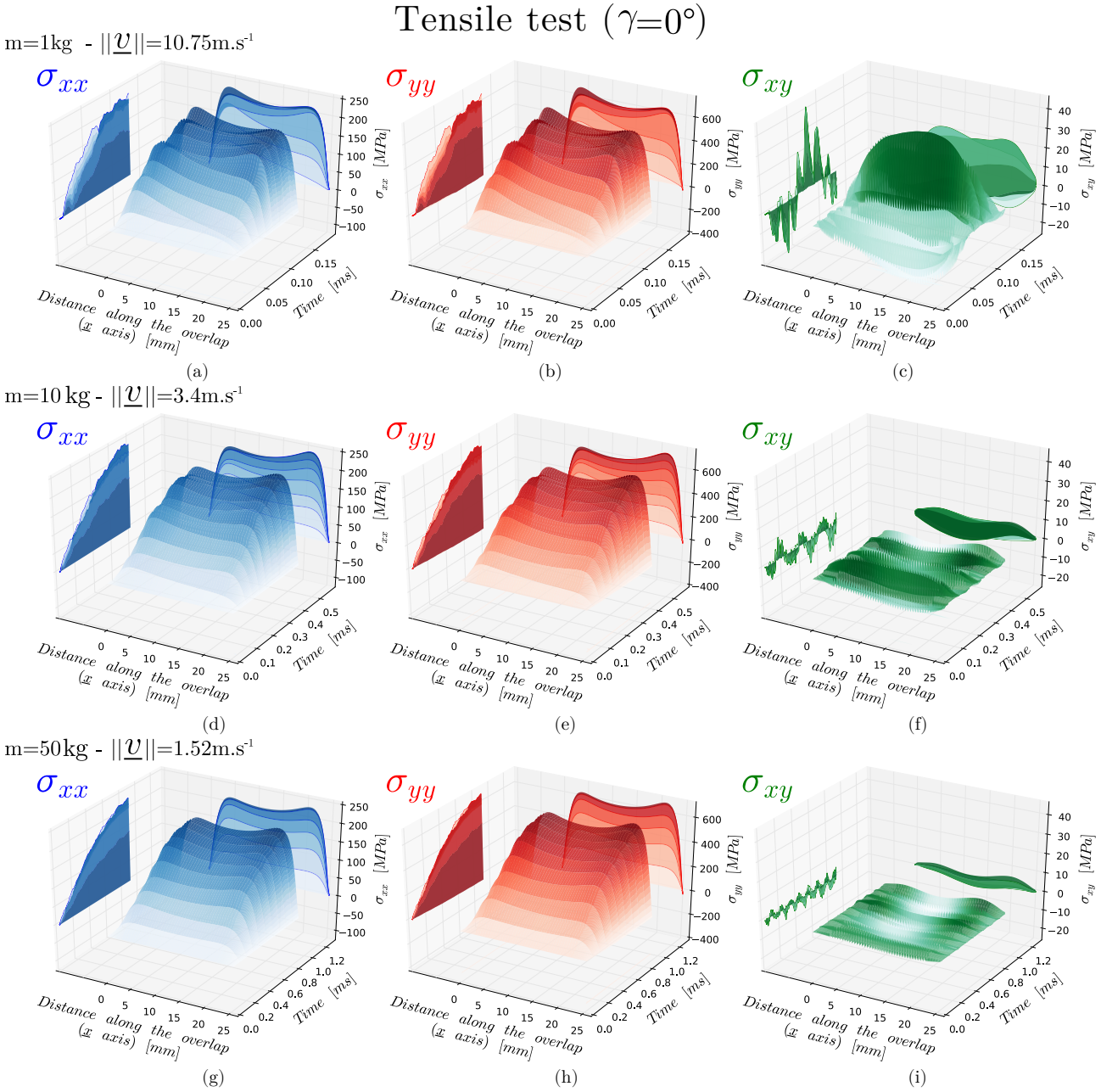

Figure 12: The spatial *vs* temporal stress distributions in the mid-plane of the adhesive (extracted from $h = 0$) in the case of a **tensile test** for three configurations : (a-c) $m = 1\,\text{kg}$ and $\|\underline{v}\| = 10.75\,\text{m.s}^{-1}$. (d-f) $m = 10\,\text{kg}$ and $\|\underline{v}\| = 3.4\,\text{m.s}^{-1}$. (g-i) $m = 50\,\text{kg}$ and $\|\underline{v}\| = 1.52\,\text{m.s}^{-1}$. (a, d, g) σ_{xx} distributions. (b, e, h) σ_{yy} distributions. (c, f, i) σ_{xy} distributions.

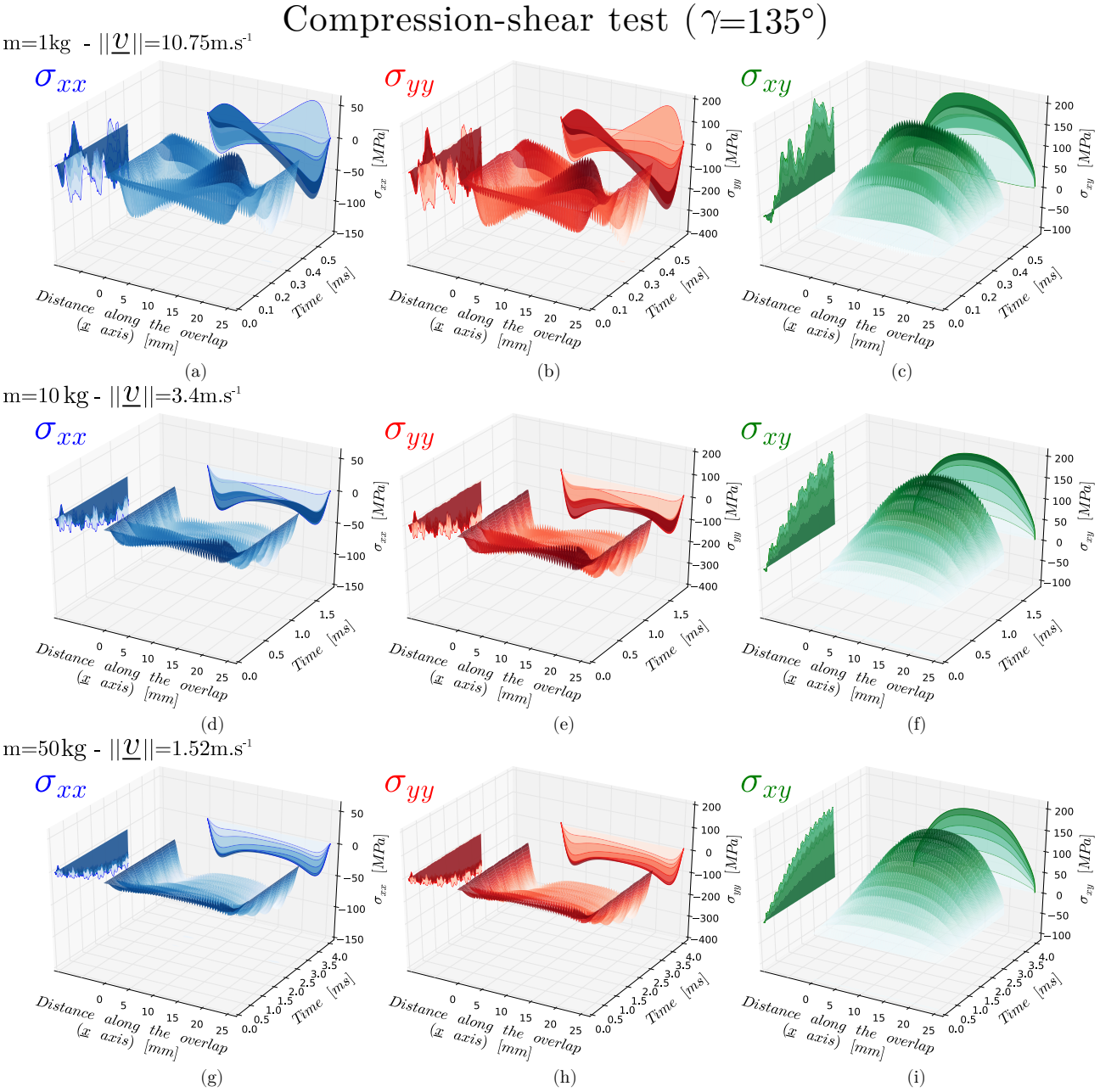

Figure 13: The spatial *vs* temporal stress distributions in the mid-plane of the adhesive (extracted from $h = 0$) in the case of a **compression-shear test** for three configurations : (a-c) $m = 1\,\text{kg}$ and $\|\underline{v}\| = 10.75\,\text{m.s}^{-1}$. (d-f) $m = 10\,\text{kg}$ and $\|\underline{v}\| = 3.4\,\text{m.s}^{-1}$. (g-i) $m = 50\,\text{kg}$ and $\|\underline{v}\| = 1.52\,\text{m.s}^{-1}$. (a, d, g) σ_{xx} distributions. (b, e, h) σ_{yy} distributions. (c, f, i) σ_{xy} distributions.

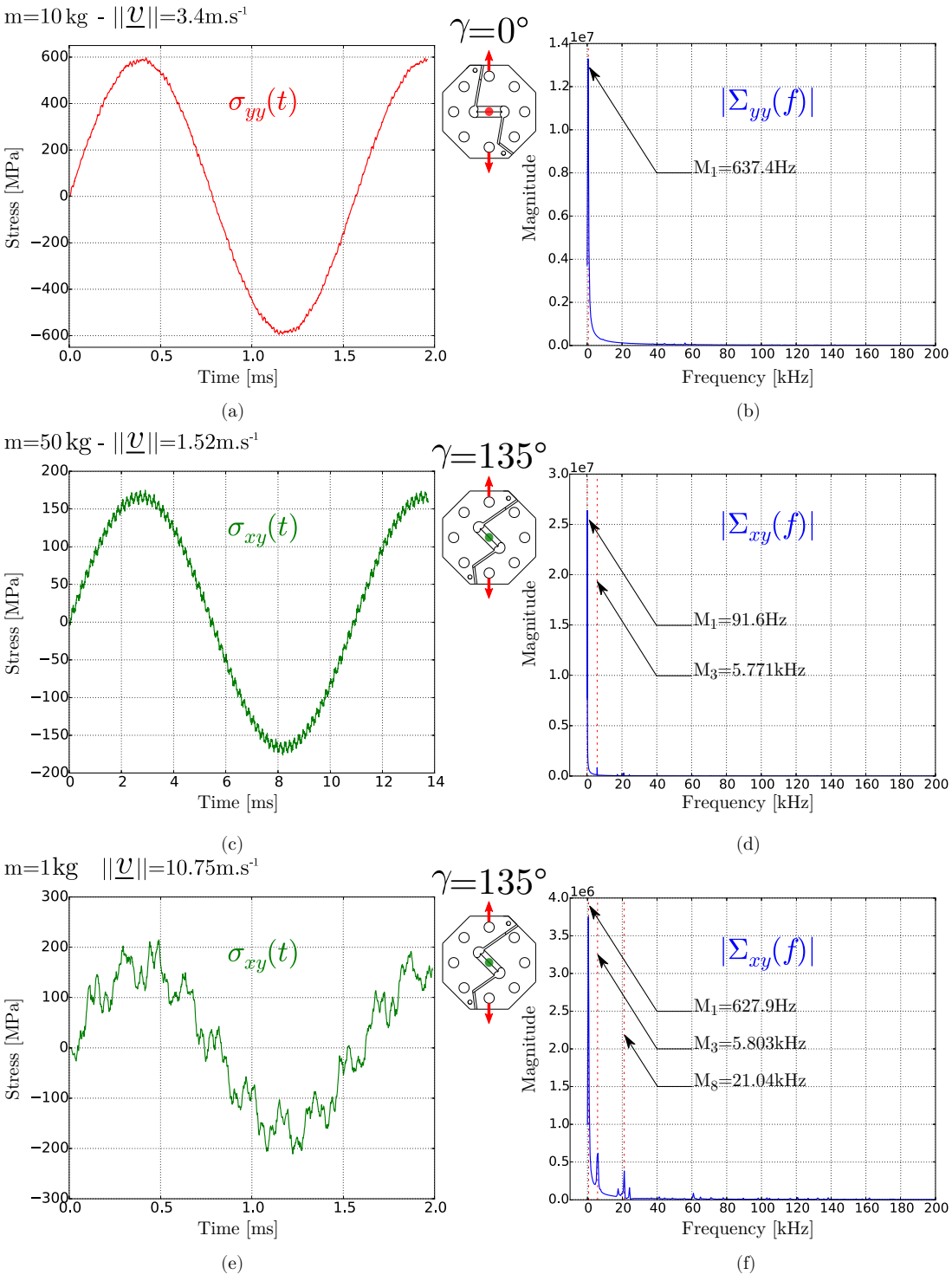

Figure 14: Modal analysis of the ARCAN TCS specimen. (a) Tensile test ($m = 10\,\mathrm{kg}$, $\|\underline{v}\| = 3.4\,\mathrm{m.s^{-1}}$). (b) Compression-shear test ($m = 50\,\mathrm{kg}$, $\|\underline{v}\| = 1.52\,\mathrm{m.s^{-1}}$). (c) Compression-shear test ($m = 1\,\mathrm{kg}$, $\|\underline{v}\| = 10.75\,\mathrm{m.s^{-1}}$).

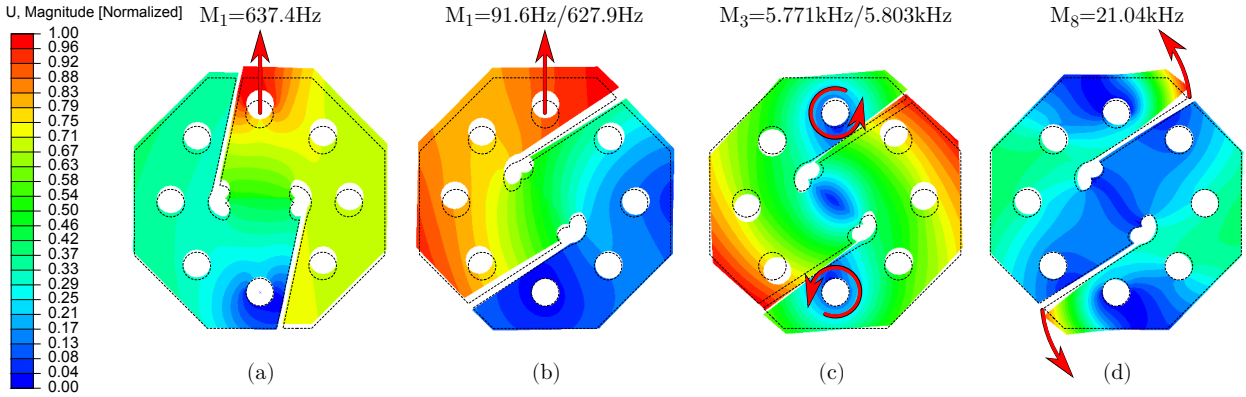

Figure 15: Main excited vibration modes. (a) Tensile loading. (b-d) Compression-shear loading.